

# A Study of Shell Model Neutron States in $^{207,209}Pb$ Using the Generalized Woods-Saxon plus Spin-Orbit Potential

J. A. Liendo,\* E. Castro, and R. Gómez

*Physics Department, Simón Bolívar University, Apdo. 89000, Caracas 1086, Venezuela*

D. D. Caussyn

*Physics Department, Florida State University, Tallahassee, Florida 32306, USA*

(Dated: July 12, 2016)

The experimental binding energies of single-particle and single-hole neutron states belonging to neutron shells that extend from  $N = 126$  to 184 and 82 to 126 respectively, have been reproduced by solving the Schrödinger equation with a potential that has two components: the generalized Woods-Saxon (GWS) potential and the spin-orbit (SO) coupling term. The GWS potential contains the traditional WS potential plus a term (SU) whose intensity reaches a maximum in the nuclear surface. Our results indicate the existence of a explicit relationship between the strength of the SU potential and the orbital angular momentum quantum number  $\ell$  of the state. This dependence has been used to make reasonable predictions for the excitation energy centroids of states located inside and outside the neutron shells investigated. Comparisons are made with results reported in previous investigations.

PACS numbers:

## 1. INTRODUCTION

Single-particle and single-hole neutron states have been previously investigated in the region around the doubly-magic  $^{208}Pb$  nucleus [1–6]. The interaction of a neutron with the rest of the nucleus referred to as the core has been represented in these studies by a Hamiltonian containing a nuclear Woods-Saxon (WS) potential[7] and a spin-orbit (SO) coupling term. Although the same potential parameterization has been used in Refs. [1–4], a unique set of parameter values has not been found. In fact, none of the reported parameterizations, including the one published by Schwierz et al.[5], has been able to produce an overall agreement between the predicted single-particle and single-hole neutron state energies and the corresponding experimental values.

In this work, we have used the so called generalized Woods-Saxon (GWS) potential instead of the original WS potential[7], with the expectation of reproducing the experimental binding energies of single-particle and single-hole neutron orbitals that exist in the neutron shells  $N = 126 – 184$  and  $82 – 126$ , respectively. This potential contains the WS potential plus a term referred to as the surface (SU) potential that maximizes in the nuclear surface and is linearly proportional to the derivative of a WS function. It is a well known fact that the WS potential alone does not reproduce the energies of  $\ell = 0$  single-particle levels with enough accuracy when applied to a wide nuclidic region [8]. Using a formalism where the Schrödinger equation is expressed in terms of the Jacobi polynomials, Göñül et al.[8] have obtained the total potential influencing a single  $\ell = 0$  neutron in a nucleus. The deduced potential (a GWS potential) contains a WS potential plus an additional term (a SU potential) that provides the flexibility to construct the surface structure of the related nucleus. The validity of the theoretical treatment presented in Ref. [8] is supported by the careful analysis of the analytical results obtained and the detailed discussion of the formalism prescriptions followed.

The GWS potential has been the object of study in different works published in the literature. Hamzavi et al. [9] have obtained solutions of the Dirac equation for a nucleon experiencing the GWS potential under the relativistic spin symmetry limit. Bayrak et al. [10] have modelled the behavior of a neutral pion in a nucleus and obtained an analytical solution of the Klein-Gordon equation for a spin = 0 particle moving in the GWS potential field. Using the Dirac equation, Candemir et al. [11] have determined negative energy eigenvalues which satisfy the boundary condition for any  $\kappa$  (spin-orbit operator eigenvalue) states of an anti-proton being subjected to the GWS potential in the pseudospin symmetry limit. Also, they have calculated the bound state energy eigenvalues of a proton moving under the GWS potential in the spin symmetry limit. These authors point out the usefulness of the SU potential to

---

\*Electronic address: [jliendo@usb.ve](mailto:jliendo@usb.ve)

examine the single-particle energy levels of a nucleon and an anti-nucleon since the interactions of the surface nucleon or anti-nucleon are very important in explaining the energy spectrum of the nuclei.

The SU term of the GWS potential has been shown in some cases to generate an additional potential pocket in the nuclear surface region that is crucial to understand the elastic scattering of several nuclear reactions [12, 13]. In other cases, the SU potential does not induce this potential pocket as in the heavy ion elastic scattering analysis of I. Boztosun [14] where the inclusion, within the framework of the optical potential, of two small real SU potentials, was absolutely necessary to reproduce the elastic scattering data especially at large angles. In this case, although the SU potentials do not produce pockets, they generate interference effects that lead to an impressive reproduction of the experimental cross section oscillations [14]. The potential pocket mentioned here has also been obtained theoretically by Koura et al. [15] from the study of a refined WS potential that has a term that increases the freedom in the surface structure of the potential.

C. Berkdemir et al. [16] used the Schrödinger equation with the GWS potential to generate the binding energies of several  $\ell = 0$  states of a hypothetical nucleus formed by a valence neutron plus an inert core of 56 nucleons. Unfortunately, the eigenvalue equation reported in this publication was later on shown to be physically incorrect [17]. However, the numerical calculations included in Ref. [17] show that the addition of the SU term to the WS potential allows the modification of the binding energies of  $\ell = 0$  states that otherwise would not be possible with the addition of a SO potential only. Recently, Bayrak et al. [18] examined the bound state solution of the radial Schrödinger equation with the GWS potential using the Pekeris approximation in terms of an appropriate boundary condition for arbitrary  $\ell$  states. From the closed form obtained for the energy eigenvalues, these authors calculated single-particle energies corresponding to a neutron orbiting around the  $^{56}Fe$  nucleus that are comparable to the numerical results for  $\ell = 0$ .

In this work, we use the GWS+SO potential mentioned above (GWS = WS + SU) to reproduce the experimental binding energies of zero and nonzero  $\ell$  states in  $^{209}Pb$  and  $^{207}Pb$ . The WS and SO parameter values have been taken from the work published by Schwierz et al. [5]. For every state analyzed, we have obtained the strength of the SU potential that makes coincide the theoretical binding energy with the corresponding measured value. The experimental binding energies have been extracted from previously reported neutron transfer reaction experiments carried out on  $^{208}Pb$  [19–22] and the theoretical binding energies have been obtained by solving the Schrödinger equation with the computer program GAMOW [23]. The strength of the SU potential has been shown to be a function of the orbital angular momentum of the state. This dependence has been used to predict the excitation energies of some states that lie inside and outside the neutron shells investigated.

## 2. THE TRADITIONAL WOODS-SAXON PLUS SPIN-ORBIT POTENTIAL

### 2.1. Formalism

As a starting point, we used a nuclear potential given by

$$V(r) = V_{WS}(r) + V_{SO}(r), \quad (1)$$

where the  $V_{WS}(r)$  and  $V_{SO}(r)$  potentials have the analytical expressions

$$V_{WS}(r) = -\frac{V_{WS}}{1 + \exp\left(\frac{r-R}{a}\right)}, \quad (2)$$

and

$$V_{SO}(r) = -\frac{\lambda}{4} \lambda_C^2 \frac{1}{r} \frac{d\tilde{V}_{SO}}{dr} \left[ j(j+1) - \ell(\ell+1) - \frac{3}{4} \right]. \quad (3)$$

Here,  $\lambda$  is a dimensionless parameter related to the depth of the SO potential and  $\lambda_C$  is the reduced Compton wavelength of the nucleon-core system given in fm units by

$$\lambda_C = \frac{\hbar}{\mu c} = 0.210019 \left( 1 + \frac{m_n}{M_{core}} \right), \quad (4)$$

$$\tilde{V}_{SO}(r) = -\frac{V_{SO}}{1 + \exp\left(\frac{r-R_{SO}}{a_{SO}}\right)}, \quad (5)$$

$$R = r_0 A^{1/3}, \quad \text{and} \quad R_{SO} = r_{SO} A^{1/3}. \quad (6)$$

TABLE I: Experimental ( $^{s.p.}B_{n\ell j}$ ) and theoretical ( $^{s.p.}B_{th,n\ell j}$ ) binding energies of single-particle neutron states in  $^{209}Pb$ . The experimental binding energies were obtained from the expression  $^{s.p.}B_{n\ell j} = -3.9374 + E_{n\ell j}(209)$ , where the energy centroid of each orbital,  $E_{n\ell j}(209)$ , is assumed to be equal to the excitation energy of only one excited state in  $^{209}Pb$  since the spectroscopic factor ( $C^2 S/(2j + 1)$ ) measured by Kovar et al. [20] for each  $^{209}Pb$  state, is close to 1.

orbital $\ell$ (n $\ell$ j)	$E_{n\ell j}(209)$ (MeV)	$C^2 S/(2j + 1)$	$^{s.p.}B_{n\ell j}$ (MeV)	$^{s.p.}B_{th,n\ell j}$ (MeV)
$2g_{9/2}$	4 0.000	0.83	-3.937	-3.822
$1i_{11/2}$	6 0.779	0.86	-3.158	-2.699
$3d_{5/2}$	2 1.565	0.98	-2.372	-1.915
$4s_{1/2}$	0 2.033	0.98	-1.904	-1.382
$2g_{7/2}$	4 2.492	1.05	-1.445	-1.117
$3d_{3/2}$	2 2.537	1.07	-1.400	-0.945

TABLE II: A comparison between the experimental ( $^{s.p.}B_{n\ell j}$ ) and theoretical ( $^{s.p.}B_{th,n\ell j}$ ) binding energies of the  $1j_{15/2}$  orbital in  $^{209}Pb$  determined for different fragmentation schemes. The experimental energies were determined by evaluating Eq. (8). The theoretical energies were calculated with the computer program GAMOW [23] using the potential given in Eq. (1). The excitation energies of the  $^{209}Pb$  fragments,  $E_x(209)$ , and their spectroscopic factors,  $C^2 S / (2j + 1)$ , were extracted from an investigation of the  $^{208}Pb(d, p)$  reaction at  $E_{lab}(d) = 20$  MeV [20]. For the scheme 1, the energy centroid  $E_{n\ell j}(209)$  was assumed to be equal to the  $^{209}Pb$  excitation energy  $E_x(209) = 1.424$  MeV. The schemes 2 and 3 include four  $^{209}Pb$  fragments. The deuteron break up potential was used to generate the results corresponding to the scheme 3.

Fragmentation Scheme	$E_x(209)$ (MeV)	$C^2 S/(2j + 1)$	$E_{n\ell j}(209)$ (MeV)	$^{s.p.}B_{n\ell j}$ (MeV)	$^{s.p.}B_{th,n\ell j}$ (MeV)
1	1.424	1.00	1.424	-2.513	-2.369
2	1.424	0.58	1.782	-2.155	-2.369
	3.052	0.070			
	3.556	0.032			
	3.716	0.032			
3	1.424	0.77	1.769	-2.168	-2.369
	3.052	0.09			
	3.556	0.04			
	3.716	0.04			

In these equations,  $\mu$  represents the reduced mass of the neutron-core system,  $m_n$  and  $M_{core}$  are the neutron and core masses respectively,  $\hbar$  is Planck's constant divided by  $2\pi$ , and  $c$  is the speed of light. The quantum numbers  $\ell$  and  $j$  correspond to the orbital and total angular momenta respectively of a single-particle or a single-hole state.  $V_{WS}$ ,  $R$  and  $a$  represent the depth, width and surface diffuseness respectively of the WS potential. The parameters corresponding to the SO potential are  $\lambda V_{SO}$ ,  $R_{SO}$ , and  $a_{SO}$  respectively. We selected the parameterization published by Schwierz et al. [5]

$$V_{WS} = V_0 \left(1 + \frac{\kappa}{A} [-(N - Z + 1) + 2]\right) , \quad V_{SO} = V_0 , \quad (7)$$

and the parameter values:  $V_0 = 52.06$  MeV,  $\kappa = 0.639$ ,  $r_0 = 1.260$  fm,  $r_{SO} = 1.16$  fm,  $a = a_{SO} = 0.662$  fm and  $\lambda = 24.1$ . This WS + SO parameterization is applicable over the whole nuclear chart for nuclides between  $^{16}O$  and the heaviest elements, and provides a relatively good description of the nuclear mean field leading to quality single-particle and single-hole spectra, nuclear radii, prediction of drip-lines, shell closures and other properties.

To calculate the binding energy of single-particle neutron states, the  $^{209}Pb$  nucleus ( $A = 209$ ,  $Z = 82$  and  $N = 127$ ) is considered as a system formed by a valence neutron and a core of 208 nucleons, equivalent to the doubly-magic  $^{208}Pb$  nucleus. The reduced Compton wavelength (Eq. (4)) is calculated with  $m_n = 1.0087$  u and  $M_{core} = 207.9767$  u. For the determination of the single-hole neutron state energies, the  $^{207}Pb$  nucleus is treated as a  $^{208}Pb$  nucleus minus one neutron or, equivalently, a core of 207 nucleons ( $M_{core} = 206.9759$  u) plus a neutron-hole. Since a single-hole state can be considered as an unoccupied single-particle state, the WS and SO widths and strengths, used to obtain the binding energies of hole (unoccupied) states in  $^{207}Pb$ , are determined with the values  $A = 208$ ,  $Z = 82$  and  $N = 126$ .

TABLE III: Experimental ( $^{s.h.}B_{n\ell j}$ ) and theoretical ( $^{s.h.}B_{th,n\ell j}$ ) binding energies of single-hole neutron states in  $^{207}Pb$ . The experimental binding energies were obtained from the expression  $^{s.h.}B_{n\ell j} = -7.3678 - E_{n\ell j}(207)$ , where  $E_{n\ell j}(207)$  represents the excitation energy centroid of each orbital. The excitation energies of the  $^{207}Pb$  fragments,  $E_x(207)$ , and their spectroscopic factors,  $C^2 S/(2j+1)$ , were extracted from Ref. [22] for the  $3p_{1/2}$ ,  $2f_{5/2}$  and  $3p_{3/2}$  states and from Ref. [21] for the rest of the states.

orbital	$\ell$	$E_x(207)$	$C^2 S/(2j+1)$	$E_{n\ell j}(207)$	$^{s.h.}B_{n\ell j}$	$^{s.h.}B_{th,n\ell j}$
(n $\ell$ j)		(MeV)		(MeV)	(MeV)	(MeV)
$3p_{1/2}$	1	0.000	1.1	0.000	-7.368	-7.687
$2f_{5/2}$	3	0.570	0.88	0.570	-7.938	-8.412
$3p_{3/2}$	1	0.900	0.96	0.900	-8.268	-8.492
$1i_{13/2}$	6	1.629	0.857	1.869	-9.237	-9.332
			5.990	0.050		
$2f_{7/2}$	3	2.334	0.913	2.913	-10.281	-10.716
			4.572	0.044		
			4.765	0.035		
			6.370	0.113		
$1h_{9/2}$	5	3.415	0.690	4.014	-11.382	-10.681
			3.660	0.090		
			5.410	0.112		
			5.620	0.180		
$1h_{11/2}$	5	7.010	0.088	8.077	-15.445	-15.906
			7.590	0.088		
			7.960	0.064		
			8.220	0.055		
			8.540	0.077		
			9.220	0.088		

The single-particle neutron orbitals studied in this work ( $2g_{9/2}$ ,  $1i_{11/2}$ ,  $1j_{15/2}$ ,  $3d_{5/2}$ ,  $4s_{1/2}$ ,  $2g_{7/2}$  and  $3d_{3/2}$ ) lie above the Fermi level, belong to a neutron shell that extends from  $N = 126$  to 182, and all of them except the  $1j_{15/2}$  orbital have even  $\ell$  values and positive parity. In contrast, the single-hole neutron orbitals ( $1h_{11/2}$ ,  $1h_{9/2}$ ,  $2f_{7/2}$ ,  $1i_{13/2}$ ,  $3p_{3/2}$ ,  $2f_{5/2}$  and  $3p_{1/2}$ ) are located below the Fermi level, all of them except the  $1h_{11/2}$  level belong to the  $N = 82 - 126$  shell, and all of them except the  $1i_{13/2}$  orbital have odd  $\ell$  values and negative parity. We used the computer code GAMOW [23] with some minor modifications to calculate the binding energies of all these orbitals. The theoretical results obtained have been compared with the experimental single-particle and single-hole binding energies,  $^{s.p.}B_{n\ell j}$  and  $^{s.h.}B_{n\ell j}$ , given respectively by

$$^{s.p.}B_{n\ell j} = \Delta M(209) - \Delta M(208) - \Delta M_n + E_{n\ell j}(209) , \quad (8)$$

and

$$^{s.h.}B_{n\ell j} = \Delta M(208) - \Delta M(207) - \Delta M_n - E_{n\ell j}(207) , \quad (9)$$

where  $\Delta M_n$ ,  $\Delta M(209)$ ,  $\Delta M(208)$  and  $\Delta M(207)$  are the neutron,  $^{209}Pb$ ,  $^{208}Pb$  and  $^{207}Pb$  mass excesses equal to 8.0713, -17.6153, -21.7492 and -22.4527 MeV respectively. The energy  $E_{n\ell j}(209)$  ( $E_{n\ell j}(207)$ ) represents the excitation energy centroid in  $^{209}Pb$  ( $^{207}Pb$ ) around which the strength of a single-particle (single-hole) neutron orbital (characterized by the quantum numbers  $n$ ,  $\ell$ , and  $j$ ) is fragmented.

## 2.2. Results

Table I depicts the theoretical binding energies,  $^{s.p.}B_{th,n\ell j}$ , determined with the GAMOW code [23] for the single-particle neutron orbitals  $2g_{9/2}$ ,  $1i_{11/2}$ ,  $3d_{5/2}$ ,  $4s_{1/2}$ ,  $2g_{7/2}$  and  $3d_{3/2}$ , using the potential given by Eq. (1). Although the lead isotopes have been extensively investigated since the beginning of nuclear physics, little experimental data on the fragmentation of these orbitals is available in the literature [19]. These orbitals have been predicted by the

shell model and observed in single-particle stripping reactions on  $^{208}Pb$  [19]. Based on a meticulous investigation of the  $^{208}Pb(d, p)^{209}Pb$  reaction at  $E_{lab} = 20$  MeV carried out by Kovar et al. [20] and the results of different neutron stripping reaction studies compiled by Martin [19], the strength of each one of these single-particle states may be considered as mostly concentrated in one excited state of the  $^{209}Pb$  nucleus. In order to determine each experimental binding energy  $^{s,p}B_{n\ell j}$  shown in Table I, we assumed that each excitation centroid  $E_{n\ell j}(209)$  used to evaluate Eq. (8), was equal to a particular  $^{209}Pb$  excitation energy.

Table II contains different values determined for the experimental binding energy of the  $1j_{15/2}$  orbital assuming three fragmentation schemes. From the study of the  $^{208}Pb(\alpha, ^3He)$  reaction at  $E_{lab}(\alpha) = 183$  MeV, Massolo et al. [21, 24] demonstrated the strong population of the  $1j_{15/2}$  single-particle level at 1.424 MeV excitation energy in  $^{209}Pb$  and the existence of fragments up to 5 MeV. In the first fragmentation scheme considered in Table II, the  $1j_{15/2}$  strength is assumed to be concentrated completely at 1.424 MeV excitation energy. The schemes 2 and 3 include three fragments, in addition to the 1.424 MeV state, that, according to Kovar et al. [20], exhaust most of the available  $1j_{15/2}$  single-particle strength. Although these schemes include the same fragments, their corresponding spectroscopic factors, extracted from a DWBA analysis of the  $^{208}Pb(d, p)$  reaction at  $E_{lab}(\alpha) = 20$  MeV, are different because the deuteron break up potential was only included in the scheme 3.

Table III displays experimental and theoretical binding energies of the single-hole neutron states in  $^{207}Pb$  studied in the current work. Angular distributions of cross sections and analyzing powers corresponding to the ground ( $1/2^-$ ), 0.570 MeV ( $5/2^-$ ) and 0.900 MeV ( $3/2^-$ ) states in  $^{207}Pb$  were measured by Matoba et al. [22] in a study of the  $^{208}Pb(p, d)^{207}Pb$  reaction at  $E_{lab} = 65$  MeV. The spectroscopic factors obtained for these states indicate that the strengths of the  $3p_{1/2}$ ,  $2f_{5/2}$  and  $3p_{3/2}$  orbitals are about 90 %. These spectroscopic factors are consistent with the predictions of the particle-vibration coupling model published by Majumdar [25]. The experimental fragmentation data corresponding to the  $1i_{13/2}$ ,  $2f_{7/2}$ ,  $1h_{9/2}$  and  $1h_{11/2}$  orbitals were extracted from a study of the  $^{208}Pb(^3He, \alpha)^{207}Pb$  reaction at  $E_{lab} = 70$  MeV carried out by Galès et al. [21].

The theoretical binding energies presented in Tables I and III for the  $4s_{1/2}$ ,  $3d_{3/2}$ ,  $3d_{5/2}$ ,  $3p_{1/2}$  and  $3p_{3/2}$  orbitals are consistent with those calculated by Wang et al. [6] using an elaborately constructed multi-step potential to approximate the WS + SO potential specified in Eq. (3). However, no agreement exists between any of the theoretical predictions and the corresponding experimental value, similarly to what has been reported in the literature [1–5]. As shown in Tables I and II, the theoretical binding energies of the single-particle neutron states are in general less negative than the corresponding experimental values. The opposite occurs for the single-hole neutron states displayed in Table III. This is a consequence of how Schwierz et al. [5] obtained the parameter values  $V_0 = 52.06$  MeV and  $\kappa = 0.639$ , used in the current work to evaluate Eq. (7). These parameters were optimized by using a set of  $V_0$  and  $\kappa$  values corresponding to single-particle and single-hole neutron and proton states present in the vicinity of the doubly-magic nuclei  $^{16}O$ ,  $^{40}Ca$ ,  $^{48}Ca$ ,  $^{56}Ni$ ,  $^{100}Sn$ ,  $^{132}Sn$  and  $^{208}Pb$ .

### 3. THE GENERALIZED WOODS-SAXON PLUS SPIN-ORBIT POTENTIAL

#### 3.1. Formalism

In order to correct the differences mentioned in Section 2.2, between experimental and theoretical energy values, we have replaced the traditional Woods-Saxon potential  $V_{WS}(r)$  contained in Eq. (1) by the Generalized Woods-Saxon potential  $V_{GWS}(r)$  [9–11, 16–18], given by

$$V_{GWS}(r) = V_{WS}(r) + V_{SU}(r), \quad (10)$$

where  $V_{SU}(r)$  is a surface potential, proportional to a derivative of a Woods-Saxon function, and given by

$$V_{SU}(r) = - C_{\ell j} \frac{\exp\left(\frac{r-R}{a}\right)}{\left(1+\exp\left(\frac{r-R}{a}\right)\right)^2} . \quad (11)$$

The parameter  $a$  was defined previously,  $R$  is given by Eq. (6) and the value of  $C_{\ell j}$  is calculated for each orbital when the theoretical binding energy coincides with the experimental value.

#### 3.2. Results

Table IV contains the  $C_{\ell j}$  values obtained for all the single-particle and single-hole neutron states studied here. The positive (negative) signs of  $C_{\ell j}$  determined for single-particle (single-hole) states are, in part, a consequence of the

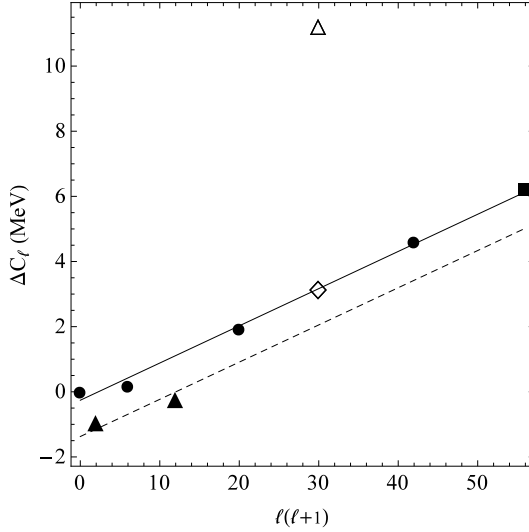


FIG. 1:  $\Delta C_\ell = C_{(j=\ell-1/2)} - C_{(j=\ell+1/2)}$  vs.  $\ell(\ell+1)$ . The solid line (Eq. (14)) was generated with the  $\Delta C_\ell$  values of the s, d, g and i orbitals (circles). The  $\Delta C_\ell$  values obtained for the p and f orbitals (solid triangles) lie close to a dashed line which is equal to the solid line minus 1.1142 MeV. The determination of the empty triangle was based on the excitation energy centroids measured by Galès [21] for the h orbitals. The square and the diamond are explained in the text.

parameterization Eq. (7), and the associated parameter values [5]. We have also included in the table, the average  $\bar{C}_\ell$  and the difference  $\Delta C_\ell$  of every pair of  $C_{\ell j}$  values ( $j = \ell \pm 1/2$ ) corresponding to the same quantum number  $\ell$ . They are given by

$$\Delta C_\ell = C_{(j=\ell-1/2)} - C_{(j=\ell+1/2)} \quad , \quad (12)$$

and

$$\bar{C}_\ell = [C_{(j=\ell-1/2)} + C_{(j=\ell+1/2)}]/2 \quad . \quad (13)$$

Since the beginning of this investigation, we had the idea of finding a mathematical expression to connect the strength  $C_{\ell j}$  of the SU potential with a physical quantity relevant to the problem. After a time consuming process of trial and error, we finally realized that when the differences  $\Delta C_\ell$  (see Table IV) associated to  $\ell = 0, 2, 4$  and  $6$  (solid circles in Fig. 1) are plotted as a function of the emblematic quantity  $\ell(\ell+1)$ , they align along the straight solid line shown in Fig. 1. Surprisingly, the four solid circles displayed in Fig. 2 (corresponding to the  $\bar{C}_\ell$  values for  $\ell = 0, 2, 4$  and  $6$ , plotted as a function of  $\ell(\ell+1)$ ) belong to the same parabola (solid curve shown in Fig. 2). These results together with the fact that  $\bar{C}_\ell$  and  $\Delta C_\ell$  are independent variables, support the existence of a formula that describes the strength  $C_{\ell j}$  in terms of  $\ell(\ell+1)$ . The circles shown in Figs. 1 and 2, are nicely described by the solid curves given by

$$\Delta C_\ell = 0.1142\ell(\ell+1) - 0.2592 \quad , \quad (14)$$

and

$$\bar{C}_\ell = 0.0058[\ell(\ell+1)]^2 - 0.3851\ell(\ell+1) + 7.52 \quad . \quad (15)$$

The squares, triangles and diamonds included in the figures will be explained in detail later.

The impressive agreement observed between the circles and the solid curves shown in Figs. 1 and 2, allowed the determination of the  $C_{\ell j}$  value corresponding to the  $1j_{13/2}$  orbital. This state lies above the shell  $N = 126 - 184$ . Evaluating Eqs. (14) and (15) for  $\ell = 7$ , we obtained  $\bar{C}_{(\ell=7)} = 4.080$  MeV and  $\Delta C_{(\ell=7)} = 6.127$  MeV. In accordance with the notation used in Eqs. (12) and (13),  $C_{(j=13/2)} = C_{(j=7-1/2)}$  represents the  $C_{\ell j}$  value of the  $1j_{13/2}$  orbital. In principle,  $C_{(j=15/2)}$  may be any of the three  $C_{\ell j}$  values displayed in Table IV for the  $1j_{15/2}$  orbital. It is important to realize that two  $C_{(j=13/2)}$  values can be determined independently from Eqs. (12) and (13) when one of the possible  $C_{(j=15/2)}$  values is substituted into these equations. This independence allowed us to rule out the values  $C_{(j=15/2)}$

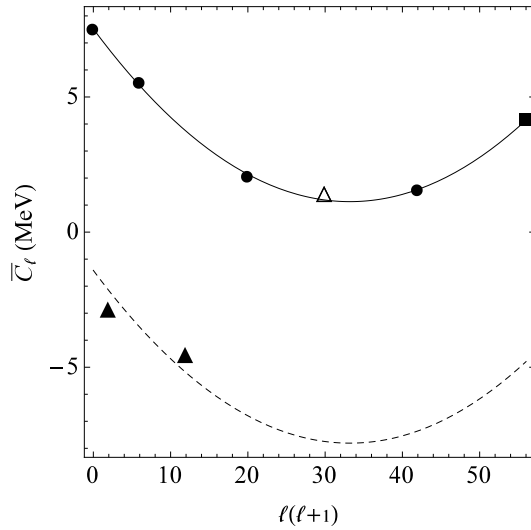


FIG. 2:  $\bar{C}_\ell = (C_{j=\ell-1/2} + C_{j=\ell+1/2})/2$  vs.  $\ell(\ell+1)$ . The solid line (Eq. (15)) was generated with the  $\bar{C}_\ell$  values of the s, d, g and i orbitals (circles). The  $\bar{C}_\ell$  values obtained for the p and f orbitals (solid triangles) lie close to a dashed curve which is equal to the solid line minus 8.9355 MeV. The determination of the empty triangle was based on the excitation energy centroids measured by Galès [21] for the h orbitals. The square is explained in the text.

$= -1.413$  and  $-1.505$  MeV (corresponding to the fragmentation schemes 2 and 3 respectively of the  $1j_{15/2}$  orbital) since the two  $C_{(j=13/2)}$  values obtained from these equations (for either  $C_{(j=15/2)} = -1.413$  or  $-1.505$  MeV) were different. On the contrary, the  $C_{(j=13/2)}$  values obtained by evaluating Eqs. (12) and (13) with  $C_{(j=15/2)} = 1.004$  MeV (associated to the fragmentation scheme 1 of the  $1j_{15/2}$  orbital), are close (7.131 and 7.156 MeV). Substituting the average of these  $C_{(j=13/2)}$  values (7.143 MeV) and  $C_{(j=15/2)} = 1.004$  MeV into Eqs. (12) and (13), we obtained the values  $\bar{C}_{(\ell=7)} = 4.074$  MeV and  $\Delta C_{(\ell=7)} = 6.139$  MeV that are close to the ones specified at the beginning of this paragraph. These new  $\Delta C_{(\ell=7)}$  and  $\bar{C}_{(\ell=7)}$  values are displayed as squares in Figs. 1 and 2. The discarding of negative  $C_{(j=15/2)}$  values is consistent with the general tendency observed in the  $C_{\ell j}$  values corresponding to single-particle neutron states of being positive.

The GAMOW code [23] was run for the  $1j_{13/2}$  orbital, using the GWS+SO potential with  $C_{(j=13/2)} = 7.143$  MeV. A positive binding energy of 4.473 MeV was obtained for this unbound orbital which represents an excitation energy above the  $2g_{9/2}$  level of 8.410 MeV in  $^{209}Pb$ . In odd nuclei, such as the  $^{209}Pb$  nucleus, some excited states can be described as admixtures of single-particle states or quasiparticle states coupled to collective excitations of the even-even core [26], in this case the  $^{208}Pb$  nucleus. Previous works support the idea that the coupling of a single-particle state with surface vibrations is mainly responsible for the damping process of the single-particle mode [27–29]. Based on the so called quasiparticle-phonon model (QPM), Giai et al. [26] found (Fig. 4 of Ref. [26]) that the strength of the  $j_{13/2}$  state above 7 MeV excitation energy in  $^{209}Pb$  depends strongly on its coupling with the first  $3^-$  and  $5^-$  vibrational states in  $^{208}Pb$ . In particular, a bump obtained at 8.8 MeV excitation energy was shown to be due to the coupling with the  $5^-$  state. Similar calculations were also carried out [26] for the  $k_{17/2}$  and  $h_{11/2}$  states in  $^{209}Pb$  and a QPM inclusive spectrum that included the strength functions of the  $k_{17/2}$ ,  $j_{13/2}$  and  $h_{11/2}$  states was generated and compared to the experimental  $^{208}Pb(\alpha, ^3He) ^{209}Pb$  singles spectrum measured by Beaumel et al. [30] at 120 MeV incident energy and  $0^\circ$ . The centroids of the theoretical distribution of transfer cross sections between 6 and 12 MeV excitation energy in  $^{209}Pb$ , were shown to be shifted to higher energies by approximately 0.5 MeV in comparison with the centroids observed in the experimental distribution. This indicates that the excitation energy value predicted by us at 8.410 MeV for the  $1j_{13/2}$  state may be related to the theoretical  $^{209}Pb$  fragment obtained by Giai et al. [26] at 8.8 MeV or represents the average excitation energy of all the fragments calculated between 6 and 12 MeV.

The calculation of the  $\Delta C_{(\ell=5)}$  value corresponding to the open triangle displayed in Fig. 1 is based on the  $^{207}Pb$  fragmentations (see Table III) measured by Galès et al. [21] for the  $1h_{9/2}$  and  $1h_{11/2}$  orbitals. This data point is too far from the solid curve. On the contrary, the  $\bar{C}_{(\ell=5)}$  value, shown also as an open triangle in Fig. 2, is consistent with the  $\bar{C}_\ell$  vs.  $\ell(\ell+1)$  value predicted by the solid curve. This agreement facilitated the calculation of new  $C_{\ell j}$  values for the h orbitals that are different from those displayed in Table IV. For this purpose, we substituted into Eqs. (12) and (13), the  $\bar{C}_{(\ell=5)}$  value corresponding to the open triangle of Fig. 2 and the  $\Delta C_{(\ell=5)}$  value predicted by the solid curve displayed in Fig. 1 (open diamond). We then run the GAMOW code [23] with the new  $C_{\ell j}$  values

TABLE IV:  $C_{\ell j}$  values of the surface potential  $V_{SU}$  (Eq. (11)) that make coincide the theoretical and measured binding energies of the shell model states analyzed in the current work.  $\bar{C}_\ell$  and  $\Delta C_\ell$  are the average and the difference respectively of any pair of  $C_{\ell j}$  values corresponding to a particular quantum number  $\ell$ . The results labeled by a, b and c are the  $C_{\ell j}$  values obtained for the fragmentation schemes 1, 2 and 3 respectively shown in Table II for the  $1j_{15/2}$  orbital.

orbital (n $\ell$ j)	$\ell$	$C_{\ell j}$ (MeV)	$\bar{C}_\ell$ (MeV)	$\Delta C_\ell$ (MeV)
$4s_{1/2}$	0	7.509	7.509	0
$3p_{1/2}$	1	-3.307	-2.842	-0.930
$3p_{3/2}$		-2.377		
$3d_{3/2}$	2	5.626	5.536	0.180
$3d_{5/2}$		5.446		
$2f_{5/2}$	3	-4.631	-4.522	-0.218
$2f_{7/2}$		-4.413		
$2g_{7/2}$	4	3.031	2.063	1.934
$2g_{9/2}$		1.096		
$1h_{9/2}$	5	7.055	1.436	11.238
$1h_{11/2}$		-4.183		
$1i_{11/2}$	6	3.866	1.562	4.608
$1i_{13/2}$		-0.742		
$1j_{15/2}$	7	1.004 <sup>a</sup>		
		-1.413 <sup>b</sup>		
		-1.505 <sup>c</sup>		

to determine the corresponding binding and excitation energies that are shown in Table V. Although the excitation energy centroids  $E_{n\ell j}$  displayed in this table for the  $1h_{9/2}$  and  $1h_{11/2}$  orbitals (3.590 and 8.543 MeV respectively) differ from those contained in Table III (4.014 and 8.077 MeV respectively), the new centroids lie inside the experimental excitation energy regions where Galès et al. [21] measured the fragments associated to the  $1h_{9/2}$  ( $E_x = 3.415$  to 5.620 MeV) and  $1h_{11/2}$  ( $E_x = 7.010$  to 9.220 MeV) orbitals. The very strong background present in the spectrum region where the fragments of these two h orbitals were detected [21], suggests the convenience of carrying out new strength measurements to clarify the disagreements mentioned here.

Using Eqs. (12) to (15), the strength  $C_{\ell j}$  of an orbital characterized by  $j$  and  $\ell$  can be written as

$$C_{\ell j} = C_{(j=\ell\pm 1/2)} = \alpha_{(\pm)}[\ell(\ell+1)]^2 + \beta_{(\pm)}\ell(\ell+1) + \gamma_{(\pm)} , \quad (16)$$

where  $\alpha_{(\pm)} = 0.0058$  MeV,  $\beta_{(+)} = -0.4422$  MeV,  $\beta_{(-)} = -0.328$  MeV,  $\gamma_{(+)} = 7.6496$  MeV and  $\gamma_{(-)} = 7.3904$  MeV. The convenience of expression (16) is to have an easy way of determining the  $C_{\ell j}$  value required in Eq. (11) to obtain the correct binding energy. Eq. (16) applies to all the orbitals studied here except the p and f orbitals shown as solid triangles in Figs. 1 and 2. It would be advisable to revisit the investigation of these two orbitals in the future: on the one hand, the experimental publication [22] from which the data associated to these orbitals was extracted, seems to be solid and well supported [25]. On the other hand, the  $\Delta C_\ell$  vs.  $\ell(\ell+1)$  and  $\bar{C}_\ell$  vs.  $\ell(\ell+1)$  curves depicted as solid lines in Figs. 1 and 2, impressively reproduce the data corresponding to  $\ell = 0, 2, 4$  and  $6$ , and make reasonable predictions for  $\ell = 5$  and  $7$ . We note, without currently having a good explanation for it, that the p and f triangles lie close to dashed curves obtained only by shifting the solid lines shown in Figs. 1 and 2 by 1.1142 and 8.9355 MeV respectively. Based on this, the strength  $C'_{\ell j}$  of the p and d orbitals ( $\ell = 1, 3$ ) can be expressed in terms of  $C_{\ell j}$  as

$$C'_{\ell j} = C'_{(j=\ell\pm 1/2)} = C_{(j=\ell\pm 1/2)} - \delta_{(\pm)} , \quad (17)$$

where  $\delta_+ = 8.3784$  MeV and  $\delta_- = 9.4926$  MeV.

#### 4. SUMMARY

We have used a generalized Woods-Saxon + a spin-orbit potential to reproduce the experimental binding energies of single-particle and single-hole neutron orbitals existing in the region around the doubly-magic  $^{208}Pb$  nucleus. These

TABLE V: Binding energies ( $B_{n\ell j}$ ) of  $\ell = 5, 7$  orbitals and corresponding excitation energy centroids ( $E_{n\ell j}$ ) in  $^{207}Pb$  and  $^{209}Pb$  respectively. The calculation of the  $C_{\ell j}$  values is explained in the text.

$\ell$ orbital (n $\ell$ j)	$C_{\ell j}$ (MeV)	$B_{n\ell j}$ (MeV)	$E_{n\ell j}$ (MeV)
7 $1j_{15/2}$	1.004	-2.513	1.424
$1j_{13/2}$	7.143	4.473	8.410
5 $1h_{11/2}$	0.046	-15.911	8.543
$1h_{9/2}$	2.826	-10.958	3.590

orbitals are contained in neutron shells that extend from  $N = 82$  to 126 (single-hole) and  $N = 126$  to 184 (single-particle). A remarkable agreement has been found between the binding energy values obtained by us for the  $4s_{1/2}$ ,  $3d_{3/2}$ ,  $3d_{5/2}$ ,  $3p_{1/2}$  and  $3p_{3/2}$  orbitals using the WS + SO part of the GWS + SO potential only, and those determined in a previous investigation by Wang et al. [6] following a novel theoretical approach to solve the Schrödinger equation. The WS and SO parameterization and associated parameter values were taken from a recently published work [5].

Similarly to a common outcome reported in the literature [1–6], the WS + SO part of the GWS + SO potential did not produce by itself a global agreement between theoretical and experimental energy values. We have accomplished this task with the addition of the SU potential. For each orbital characterized by  $\ell$  and  $j$ , we determined the strength  $C_{(j=\ell\pm 1/2)}$  of this potential that makes the theoretical energy (calculated with the computer program GAMOW [23]) coincide with the experimental value (determined from neutron transfer reaction experiments carried out on  $^{208}Pb$  [19–22]).

A challenging result found in this investigation is the quadratic dependence of the SU potential strength  $C_{(j=\ell\pm 1/2)}$  on the quantity  $\ell(\ell+1)$ . The physical origin of this dependence needs to be understood. It is puzzling that while the  $C_{(j=\ell\pm 1/2)}$  values corresponding to the s, d, g, h, i and j orbitals are nicely described by the quadratic expression  $C_{(j=\ell\pm 1/2)} = \alpha_{(\pm)}[\ell(\ell+1)]^2 + \beta_{(\pm)}\ell(\ell+1) + \gamma_{(\pm)}$ , the strengths of the p and f orbitals ( $C'_{(j=\ell\pm 1/2)}$ ) are relatively close to the predictions of the shifted expression  $C'_{(j=\ell\pm 1/2)} = C_{(j=\ell\pm 1/2)} - \delta_{(\pm)}$ . The different behavior exhibited by the p and f orbitals in comparison with the general tendency followed by most of the orbitals needs further investigation.

It would be important to find out if the quadratic  $\ell(\ell+1)$  dependence of  $C_{(j=\ell\pm 1/2)}$  obtained for  $^{208}Pb$ , also applies to single-particle and single-hole neutron orbitals existing around other doubly-magic nuclei such as  $^{16}O$ ,  $^{40}Ca$ ,  $^{48}Ca$ ,  $^{56}Ni$ ,  $^{100}Sn$ ,  $^{132}Sn$  and, if this is true, determine if a global quadratic function with coefficients parameterized in terms of the neutron magic numbers, could be generated. It would also be worthwhile to perform similar investigations related to single-particle and single-hole proton orbitals.

The explicit dependence of the SU potential strength on  $\ell(\ell+1)$  allowed the prediction of the binding energies of orbitals located inside and outside the neutron shells analyzed. The excitation energy obtained for the  $1j_{13/2}$  orbital may be related to the excitation energy of a  $1j_{13/2}$  fragment or the average of various fragments calculated by Giai et. [26] with the quasiparticle-phonon model where each excited state originates from the coupling of a single-particle mode with a vibrational state of the core. Based on this, we encourage the search of a formal connection, if there is any, between the  $\ell(\ell+1)$  dependence of the SU potential and the quasiparticle-phonon description or any process that may clarify the physics behind the SU potential included in this investigation. It is clear that further work is required to understand formally from a microscopic point of view the interaction mechanism responsible for the SU potential.

Although the excitation energy centroids obtained for the h orbitals studied here differ from those reported previously [21], their locations are inside the excitation energy region where the relevant  $^{207}Pb$  fragments were detected. Based on the strong background present in the spectrum where the fragments were observed [21], the remeasurement of the fragment strengths is advisable.

To the best of our knowledge, this may be the first time that the binding energies of single-particle and single-hole neutron states around  $^{208}Pb$  are successfully reproduced. This has been possible by the addition of a surface potential (quadratically dependent on  $\ell(\ell+1)$ ) to the traditional Woods-Saxon plus spin-orbit potential. In a previous investigation explained in the book by Nilsson et al. [31], the addition of a potential term (linearly dependent on  $\ell(\ell+1)$ ) to the harmonic oscillator potential make possible the reproduction of the level ordering of the finite square well potential. In the same work, an additional inclusion of a potential proportional to the dot product  $\vec{\ell} \cdot \vec{s}$  resulted in a successful reproduction of the single-neutron and single-proton level ordering measured from the spectra of nuclei near  $^{208}Pb$ . In spite of the achievement mentioned in Ref. [31], the agreement between calculated and experimental energies was not satisfactory.

It is well known that the harmonic oscillator basis has been extensively used in shell models and mean field theories for spherical and deformed nuclei [6]. Due to the asymptotic behavior, the use of this basis, especially in cases such as exotic nuclei, is questionable. The determination of the wavefunctions of a more realistic potential like it may be

the one used in this research would be a valuable task in future investigations.

## 5. ACKNOWLEDGMENTS

We wish to acknowledge the help received from graduate student Sttiwuer Díaz in the preparation of this document.

---

[1] J. Blomqvist and S. Wahlborn *Ark. Fys.* **16** (1959) 545.  
[2] E. Rost *Phys. Lett. B* **26** (1968) 184.  
[3] J. Dudek, A. Majhofer, J. Skalski, T. Werner, S. Cwiok and W. Nazarewics *J. Phys. G: Nucl. Phys.* **5** (1979) 1359.  
[4] J. Dudek, Z. Szymanski, T. Werner, A. Faessler and C. Lima *Phys. Rev. C* **26** (1982) 1712.  
[5] N. Schwierz, I. Wiedenhöver and A. Volya, nucl-th/arXiv:0709.3525v1.  
[6] G. Wang, H. Li, Y. Shen and B. Dong *J. Math. Phys.* **52** (2011) 112105.  
[7] R. D. Woods and D. S. Saxon *Phys. Rev.* **95** (1954) 577.  
[8] B. Gönül and K. Köksal *Phys. Scr.* **76** (2007) 565.  
[9] M. Hamzavi and A. A. Rajabi *ISRN High Energy Physics* **2013** (2013) 987632.  
[10] O. Bayrak and D. Sahin *Commun. Theor. Phys.* **64** (2015) 259.  
[11] N. Candemir and O. Bayrak *Mod. Phys. Lett. B* **29** (2014) 1450180.  
[12] M. E. Brandan and G. R. Satchler *Phys. Reports* **285** (1997) 143.  
[13] G. R. Satchler *Phys. Reports* **199** (1991) 147.  
[14] I. Boztosun *Phys. Rev. C* **66** (2002) 024610.  
[15] H. Koura and M. Yamada *Nucl. Phys. A* **671** (2000) 96.  
[16] C. Berkdemir, A. Berkdemir and R. Sever *Phys. Rev. C* **72** (2005) 027001.  
[17] C. Berkdemir, A. Berkdemir and R. Sever *Phys. Rev. C* **74** (2006) 039902.  
[18] O. Bayrak and E. Aciksoz *Phys. Scr.* **90** (2015) 015302.  
[19] M. J. Martin *Nuclear Data Sheets* (1991) **63** 723.  
[20] D. G. Kovar, N. Stein and C. K. Bockelman *Nucl. Phys. A* **231** (1974) 266.  
[21] S. Galès, G. M. Crawley, D. Weber and B. Zwieglinski *Phys. Rev. C* **18** (1978) 2475.  
[22] M. Matoba et al. *Phys. Rev. C* **55** (1997) 3152.  
[23] T. Vertse, K. F. Pál and Z. Balogh *Comp. Phys. Comm.* **27** (1982) 309.  
[24] C. P. Massolo, F. Azaiez, S. Galès, S. Fortier, E. Gerlic, J. Guillot, E. Hourani and J. M. Maison *Phys. Rev. C* **34** (1986) 1256.  
[25] R. Majumdar *Phys. Rev. C* **42** (1990) 631.  
[26] N. Van Giai, C. Stoyanov, V. V. Voronov and S. Fortier *Phys. Rev. C* **53** (1996) 730.  
[27] S. Galès, C. Stoyanov and A. I. Vdovin *Phys. Rep.* **166** (1988) 127.  
[28] N. Van Giai and C. Stoyanov *Phys. Lett. B* **272** (1991) 178.  
[29] V. G. Soloviev *Theory of Atomic Nuclei: Quasiparticles and Phonons* (Bristol: Institute of Physics Publishing) pp 143-245 (1992).  
[30] D. Beaumel et al. *Phys. Rev. C* **49** (1994) 2444.  
[31] S. G. Nilsson and I. Ragnarsson *Shapes and Shells in Nuclear Structure* (Cambridge: University Press) pp 54-74 (1995).